Volume 4
Number 4
April 2025
Pages 505–698

Environmental Science Advances

rsc.li/esadvances

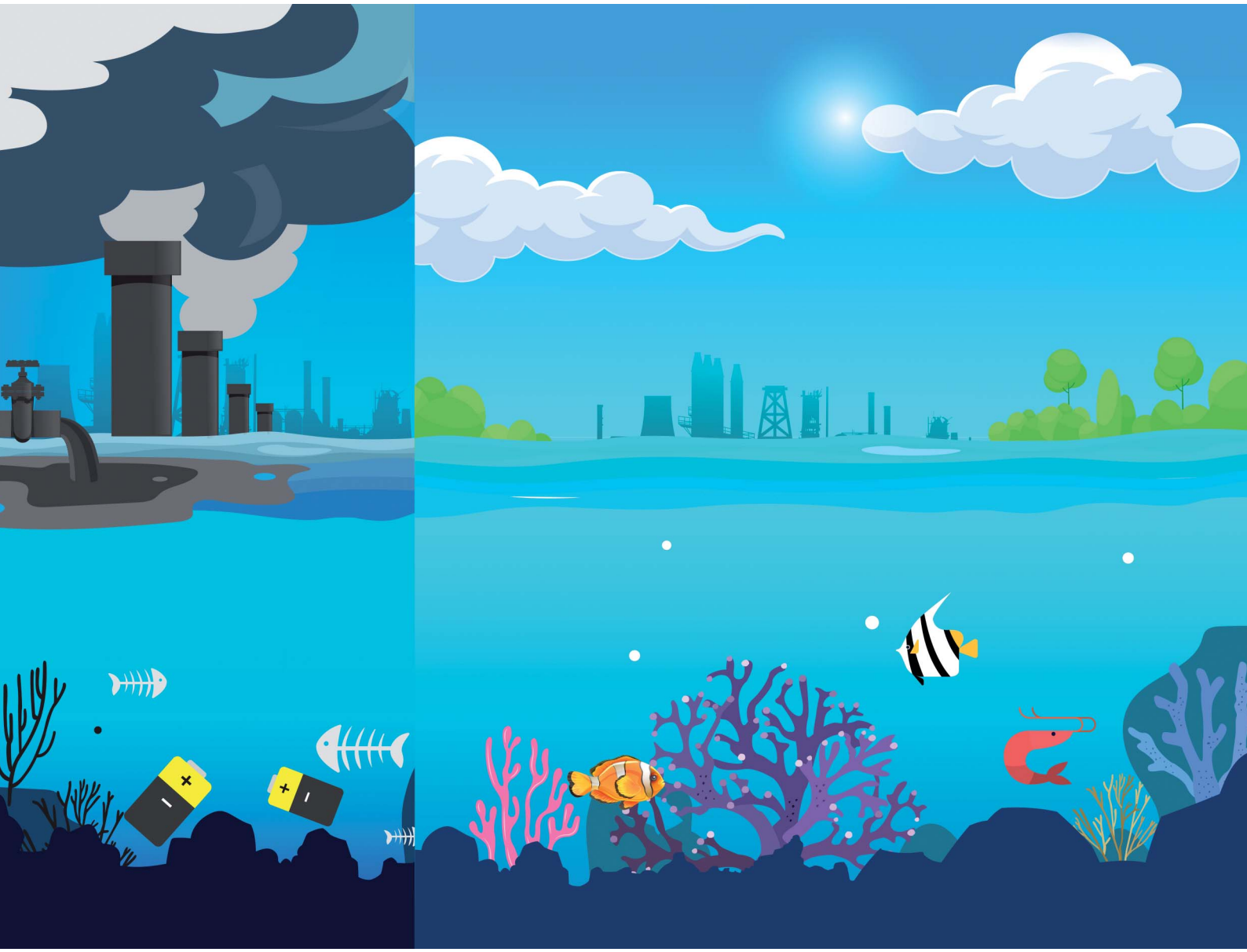

ISSN 2754-7000

ROYAL SOCIETY OF CHEMISTRY

PAPER

Md. Zahangir Alam *et al.*

Rapid adsorptive removal of Pb^{2+} ions from aqueous systems using a magnetic graphene oxide calcium alginate composite: optimisation, isotherms, and kinetics

Environmental Science Advances

ROYAL SOCIETY OF CHEMISTRY

PAPER

View Article Online
View Journal | View Issue

Cite this: *Environ. Sci.: Adv.*, 2025, **4**, 595

Rapid adsorptive removal of Pb^{2+} ions from aqueous systems using a magnetic graphene oxide calcium alginate composite: optimisation, isotherms, and kinetics†

Sadit Bihongo Malitha,[a] Dewan Md. Mahmudunnabi,[a] Shreyoshi Mazumder,[a] Khandker Saadat Hossain,[b] Mohammad Nurnabi[a] and Md. Zahangir Alam *[ac]

Water consumption from polluted sources is a significant cause of human exposure to lead compounds, posing potential risks to humans. This study investigated the synthesis and application of a magnetic graphene oxide calcium alginate composite (MGO@CA) for rapid removal of lead (Pb^{2+}) ions from aqueous systems, demonstrating its effectiveness through various adsorption studies and characterisation techniques. We utilised XRD, FTIR, VSM, and SEM to confirm the structural and magnetic properties of the MGO@CA composite, while BET and AFM analyses were performed to assess its surface area and roughness, which are essential for evaluating its adsorption capacity. Characterization results indicated the formation of a composite with functional groups of both graphene oxide and alginate and a rough surface, high surface area, and magnetic properties. The adsorption process was optimised by studying the effect of varying solution pH, adsorbent dosage, contact time, and initial lead concentration. The maximum adsorption capacity for Pb^{2+} ions was determined to be 270.27 mg g^{-1}, as revealed using the Langmuir isotherm model, indicating the high efficiency of the composite in removing lead from water. Different adsorption isotherms and reaction kinetic models were studied for the adsorption process. The obtained adsorption data fit well with both the Langmuir and Freundlich adsorption isotherms, indicating the heterogeneous surface of the composite containing sites with different affinities for Pb^{2+}. The adsorption process followed pseudo-second-order reaction kinetics. Furthermore, the adsorbent is regenerable and reusable, maintaining 82.28% of its initial adsorption capacity after 5 cycles. Thus, the MGO@CA adsorbent is remarkably efficient, ecologically sound, readily separable, and thus optimal for rapid and effective elimination of heavy metals from water.

Received 12th September 2024
Accepted 26th December 2024

DOI: 10.1039/d4va00341a

rsc.li/esadvances

Environmental significance

Heavy metal pollution in water, originating from industrial discharge and agricultural runoff, poses a significant threat to human health and the environment. Exposure to heavy metals can cause health issues, disrupt ecosystems, and harm soil as well as groundwater. They can damage the brain, kidneys, and red blood cells, which deliver oxygen throughout the body. This research shows that a magnetic graphene oxide calcium alginate composite, MGO@CA, which is derived from natural alginate, exhibits enhanced lead removal efficiency and promotes the use of eco-friendly materials. It effectively absorbs Pb^{2+} from aqueous systems and can be separated without the need for filtration. Furthermore, the magnetic properties of this composite facilitate its easy retrieval, thus minimising waste. The synthesis and application of MGO@CA are intended to be economically viable and energy-efficient, in line with sustainable methods for water treatment. Thus, the MGO@CA composite has potential as an efficient adsorbent in water treatment, with a maximum theoretical adsorption capacity of 270.27 mg g^{-1} for Pb^{2+} ions. Moreover, its high efficacy at a pH of 6 indicates its compatibility with current water treatment operations.

Introduction

Water is an essential and indispensable resource for sustaining life, and both humans and the ecosystem depend on access to clean water.[1] Any metallic element with a high density that is harmful in even small quantities is considered a heavy metal.[2] The release of substantial quantities of hazardous waste into

[a]*Department of Applied Chemistry and Chemical Engineering, University of Dhaka, Dhaka 1000, Bangladesh. E-mail: zahangir@du.ac.bd*
[b]*Department of Physics, University of Dhaka, Dhaka 1000, Bangladesh*
[c]*Atish Dipankar University of Science & Technology, Sector 15, Uttara, Dhaka, Bangladesh*

† Electronic supplementary information (ESI) available. See DOI: https://doi.org/10.1039/d4va00341a

water bodies pollutes aquatic ecosystems and modifies the chemical properties of water with heavy metal cations.[3] Lead toxicity affects plants at all stages, from germination to yield, with its impact depending on exposure time and concentration. Known as one of the first heavy metals used by humans, lead's versatility—low melting point, softness, malleability, and corrosion resistance—has made it a valuable resource for over 5000 years.[4,5] The primary sources of lead (Pb) include automobile exhaust fumes, emissions from the chimneys of factories utilizing lead, effluents from storage battery industries, and activities such as mining and smelting of lead ores. Additional contributors are processes such as metal plating and finishing, as well as the use of fertilizers, pesticides, and additives in pigments and gasoline.[6]

Daily, a variety of artificial and natural sources discharge hazardous metals into water.[1] Among them, lead (Pb) is particularly harmful in aqueous environments. This is because heavy metals tend to accumulate in aquatic animals primarily through the dissolved phase and by consuming contaminated food.[7] Fish are some of the aquatic creatures that cannot escape the negative impacts of these contaminants.[2] Consequently, their development, growth, health, and survival are impacted.[2] Heavy metal toxicity has been shown to also have lethal effects on humans, including impairment or reduction of mental and central nervous system functioning and abnormal blood composition, which can seriously harm key organs such as the kidneys and liver.[8] The average natural concentration of lead (Pb) in the soil is typically below 50 mg kg^{-1}; however, in areas near human activities, particularly abandoned mining sites, the lead levels can be significantly higher.[9]

Lead can accumulate as different salts. Experiments showed that no animals survived at the highest dose, while the control group exhibited a mean survival rate of 68%. The survival rates were higher in soils treated with $PbCl_2$ compared to that with $Pb(NO_3)_2$. Additionally, soil percolation enhanced the conditions and further improved the survival rates.[10] The concentration of Pb in contaminated sites can exceed 16 000 mg Pb per kg of dry soil, significantly beyond regulatory limitations, such as the 100 mg kg^{-1} threshold for lead in soil established by the World Health Organization (WHO).[11] In Bangladesh, over the past three decades, there has been a sharp change in Pb exposure with the rapid economic expansion.[12] A review of groundwater contamination in Bangladesh indicates that the lead concentration is in the range of 0.0006 to 3.01 mg L^{-1}. This level exceeds the safe drinking water standard set by the World Health Organization (WHO), which recommends a maximum concentration of 0.01 mg L^{-1} for lead in drinking water.[13]

Due to its particular susceptibility to contamination, addressing water pollution has become a focal point in tackling some of the most significant environmental issues.[14] Thus, for treating water, emphasis has been placed on eliminating suspended particles, processing biodegradable substances, and eradicating microorganisms.[15] Among the various water treatment methods, adsorption stands out as the predominant, cost-effective method, the effectiveness of which primarily depends on the surface characteristics, including the surface area and availability of functional groups of the utilized adsorbents.[16] Different materials such as biopolymers, activated carbon, silica, zeolites, metal–organic frameworks, and graphene-based materials have shown great potential for the removal of pollutants. Among them, graphene oxide-based composites and metal–organic frameworks such as ZIF-8 and ZIF-67, which eliminate Pb^{2+}, exhibit promise in the treatment of wastewater.[17–19]

Graphene was initially found as a thin sheet peeled from graphite, which is a flat structure made of tightly bonded carbon atoms in hexagonal patterns that show strong but breakable qualities.[20] Graphene oxide monolayers exhibit a single layer of carbon atoms with sp^2 and partial sp^3 hybridisation, featuring oxygen-containing groups on both their basal and edge planes, forming distinct regions with varying area ratios.[21] Given that GO nanosheets are hydrophilic because of their abundant oxygen-containing groups, they can be uniformly dispersed in water and polar organic solvents and facilitate the preparation of TFN (thin film nanocomposite) membranes.[22] In terms of both theory and experimentation, researchers in are becoming increasingly interested in nanofiltration membrane separation technologies, especially using graphene oxide (GO), due to their energy efficiency, high effectiveness, low cost, and tunable inter-layer spacing and honeycomb-like lattice.[23,24]

Derived from brown seaweed, alginate is a naturally occurring, negatively charged polymer that has been widely studied and utilized in various biomedical applications due to its biocompatibility, cost-effectiveness, low toxicity, and ability to form a gel with divalent cations such as Ca^{2+} at a moderate rate.[25] Due to its pollutant adsorption capability, calcium alginate can eliminate organic impurities from water and sanitise it.[26] Because sodium alginate has several noteworthy properties, such as excellent biocompatibility, biodegradability, renewability, and numerous hydroxyl and carboxyl groups with a significant affinity for heavy metal ions, adsorbents made using sodium alginate can successfully remove heavy metal ions from water.[27]

Considering this, we aimed to synthesise a magnetic graphene oxide calcium alginate composite (MGO@CA) for the fast adsorption of Pb^{2+} ions from aqueous systems. The use of calcium alginate (CA) bound GO to the polymer matrix, stopped its leaching, and preserved its adsorption capacity. Besides, making the composite magnetic greatly facilitated its separation from wastewater after the adsorption operation. The composite was characterised using different methods to study its properties. Batch adsorption studies for the removal of Pb^{2+} were carried out to determine the optimal pH and dosage, whereas different isotherms and kinetic models were thoroughly examined.

Materials and methods

Chemicals

Iron(III) chloride hexahydrate (97%) and iron(II) chloride tetrahydrate (98%) were acquired from Merck (Germany). Sodium alginate was provided by Research Lab Fine Chem. Sodium nitrate was purchased from Unichem, a supplier based in China. We acquired potassium permanganate, hydrogen

peroxide (30%), ammonia solution (25%), nitric acid (65%), hydrochloric acid (37%), and sulfuric acid (98%) from Merck (Germany). Merck (India) supplied the graphite powder (99.5%, ≤50 μm). All chemicals were employed in their original state without undergoing any further purification. We used a Laboratory Water Purification System, namely model no. SCSJ-IV, made by Biobase, to generate deionised (DI) water.

Preparation of magnetic graphene oxide calcium alginate composite (MGO@CA)

Graphene oxide was made using an improved and modified version of the Hummers' method.[28,29] Following one hour of sonication, 20 mL of water was used to dissolve 50 mg of graphene oxide (GO). Simultaneously, 14 mg of $FeCl_2 \cdot 4H_2O$ and 28 mg of $FeCl_3 \cdot 6H_2O$ were dissolved in 6 mL of water with continuous stirring, maintaining a 1 : 2 ratio. Eventually, 4 mL of a 25% ammonia solution was introduced into the mixture, leading to the formation of Fe_3O_4 magnetic particles. Given that the solution had to be neutralised (pH level 7), these particles were subjected to additional water washing. Following this, the solution that contained magnetic nanoparticles was subsequently added to the graphene oxide solution that had been dispersed earlier, and the mixture was subjected to sonication for one additional hour. In a separate beaker, which contained 50 mL of water, 35 mg of calcium carbonate and 150 mg of sodium alginate (SA) were dispersed. Subsequently, the sonicated solution of graphene oxide (GO) and magnetic nanoparticles was transferred to the same beaker. Finally, using a syringe, the resulting solution was added dropwise to a 150 mL 3% hydrochloric acid (HCl) solution. Given that the reaction had to be completed and crosslinked, the resultant composite was immersed in an acid solution for two hours.[30] Then, the solution had to be neutralised, and for this, it was repeatedly washed and freeze-dried (Fig. 1).

Characterisation

The chemical composition and physical structure of MGO@CA were characterised using field emission scanning electron microscopy (FESEM) equipped with energy-dispersive X-ray spectroscopy (EDS). The specific instrument used was a JSM-7610F model produced by JEOL in Japan. The chemical structures of MGO@CA, sodium alginate, and graphene oxide (GO) were examined using an IR Prestige-21 (FT-IR) spectrophotometer, which is manufactured by SHIMADZU, a company based in Japan. The X-ray diffraction analysis of the MGO@CA composite, GO, and SA was done on an Ultima IV multipurpose X-ray diffraction manufactured by the Rigaku Corporation in Japan. The MGO@CA surface was rough, and its intensity was measured *via* atomic force microscopy (AFM) using a Swiss Nanosurf Acoustic Enclosure 100 device. By adsorbing N_2 gas on the surface of the adsorbent, a BET Sorptometer (BET-201-A, PMI, USA) was used to measure different properties regarding the porosity of the material. Finally, using a moving sample magnetometer (MICRO-SENSE EV9, USA) at room temperature, the magnetisation hysteresis loops for the magnetic field were determined.

Fig. 1 Laboratory images of the prepared MGO@CA composite.

Batch adsorption analysis

Various factors, including initial pH, dye concentration, contact time, temperature, and adsorbent dosage, were examined to determine the optimal conditions for adsorption. Adsorption is influenced by chemical composition, pore volume, and various interactions.[19] The focus of the investigation was the adsorption of Pb^{2+} on MGO@CA. To determine the optimum pH, adsorption experiments were performed in the pH range of 2.0 to 7.0. The impact of dosage was investigated by employing an initial adsorbent dose in the range of 2.5 to 10 mg of MGO@CA. The impact of initial concentration and contact time were examined in 20, 30, and 40 ppm Pb solutions with 30, 60, 90 and 120 min contact time. The liquids were stirred at a rate of 180 rpm. A bar magnet was used to separate the adsorbent from the liquid. The Pb concentration of each solution after adsorption was determined using a PerkinElmer PinAAcle 500 Flame Atomic Absorption Spectrometer at a wavelength of 283.31 nm in an air–acetylene flame. For each sample, three replicates were analyzed.

The following equation was employed to determine the adsorption capacity, Q (mg g^{-1}):[31]

$$Q = \frac{(s_0 - s_t) \times V}{W} \quad (1)$$

where V = volume (L) of the lead solution, W = mass (g) of the adsorbent, s_0 = initial concentration of lead solution (ppm) and s_t = concentration of lead solution (ppm) at time t.

Also, the removal percentage can be determined using the following equation:[31]

$$\%\ \text{removal} = \frac{s_0 - s_t}{s_0} \times 100 \quad (2)$$

The equilibrium adsorption capacity can be determined using eqn (3), as follows:[31]

$$Q = \frac{(s_0 - s_e) \times v}{W} \quad (3)$$

were s_e = equilibrium Pb^{2+} concentration (ppm).

Result and discussion

Characterisation of prepared MGO@CA composite

The FTIR study was conducted to identify the functional groups present in both GO and MGO@CA (Fig. 2).

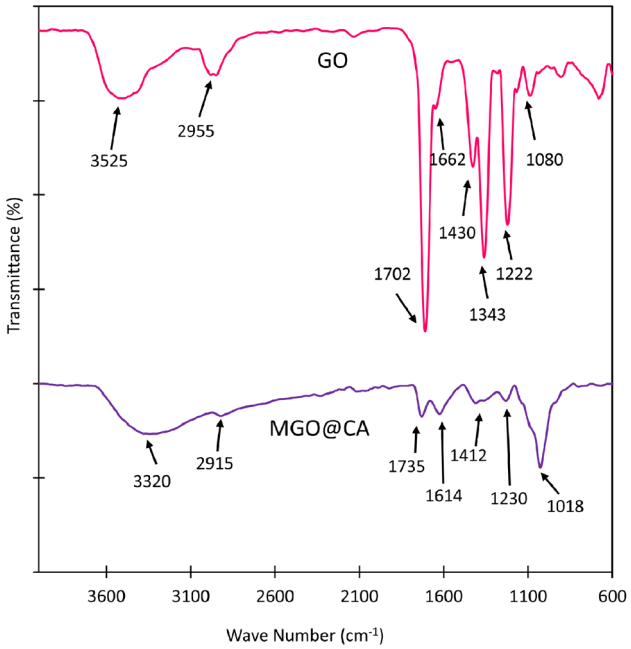

Fig. 2 FTIR spectra of GO and MGO@CA.

In the spectrum of GO, the vibrational peaks were found at 3525 cm^{-1}, 2955 cm^{-1}, 1702 cm^{-1}, 1662 cm^{-1}, 1430 cm^{-1}, 1343 cm^{-1}, 1222 cm^{-1} and 1080 cm^{-1}, as shown in Fig. 2. The peaks observed at 3525 cm^{-1} and 2955 cm^{-1} can be related to the stretching vibrations of the –OH groups and C–H bonds, while peaks at 1702 cm^{-1} and 1662 cm^{-1} were observed for the stretching of carbonyl C=O and aromatic C=C, respectively. Finally, the peaks at 1343 cm^{-1} and 1222 cm^{-1} corresponded to the C–OH and C–O stretching for the carbonyl groups, respectively. Peaks were found at 1018 cm^{-1}, 1412 cm^{-1}, 1614 cm^{-1}, 1735 cm^{-1}, 2915 cm^{-1}, and 3320 cm^{-1} for MGO@CA, which correspond to the presence of C–O–C vibrations, C–O stretching, aromatic C=C, carbonyl C=O stretching, C–H stretching and –OH groups, respectively. There was a shift in the peak for the OH group in the MGO@CA composite, which could contribute to the formation of hydrogen bonds between GO and SA.[32] The GO groups that contain oxygen were also added to the MGO@CA mixture, making it a good candidate for adsorption.[33]

The internal structure and surface morphology were studied using the images obtained from 3 different characterisation methods including FESEM, TEM, and AFM. The FESEM images were captured at different angles with varying magnifications ranging from 500 to 50 000×, which provide an all-encompassing viewpoint. According to the FESEM images, it was portrayed that the structure contained not only a fluffy and layered configuration but also some crinkled sheets (Fig. 3). The surface of the MGO@CA composite showed several stripes and was significantly rough, and these characteristics were explained by the fact that graphene oxide sheets were incorporated within the sodium alginate matrix.[34]

The EDX results of MGO@CA confirm the presence of a significant percentage of oxygen (43.37%) and iron (3.36%) together with other elements such as carbon (49.50%), sodium (0.16%), calcium (0.20%), and chlorine (3.05%) (Fig. 4).

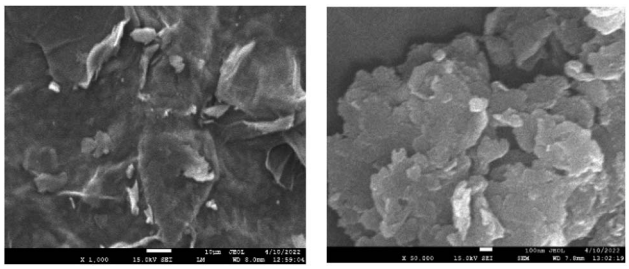

Fig. 3 FESEM images of MGO@CA.

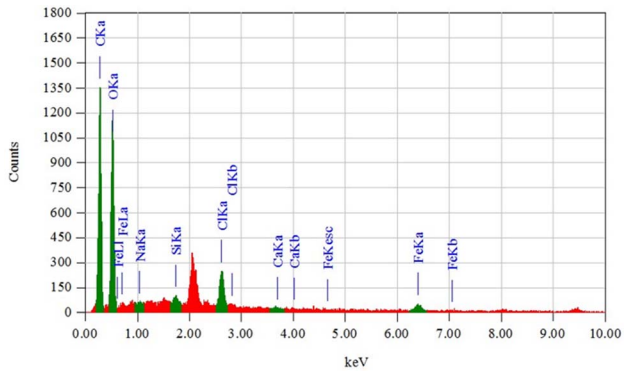

Fig. 4 EDX graph of MGO@CA.

The TEM analysis also showed the fluffy and rough structure of the MGO@CA composite (Fig. 5). It also verified the incorporation of Fe_3O_4 particles in the composite matrix.[35]

AFM imaging of MGO@CA again confirmed the formation of a rough surface in the prepared composite with an uneven surface structure. Its mean surface roughness was recorded to be 238.20 nm (Fig. 6). This high surface roughness may

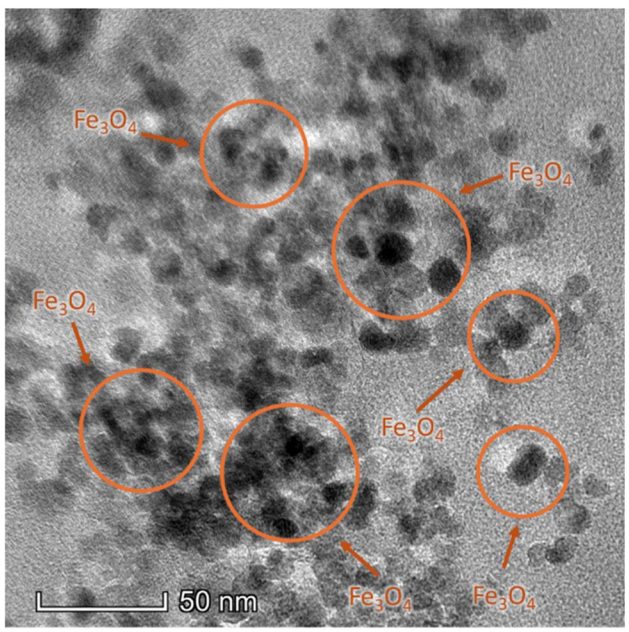

Fig. 5 TEM image of MGO@CA.

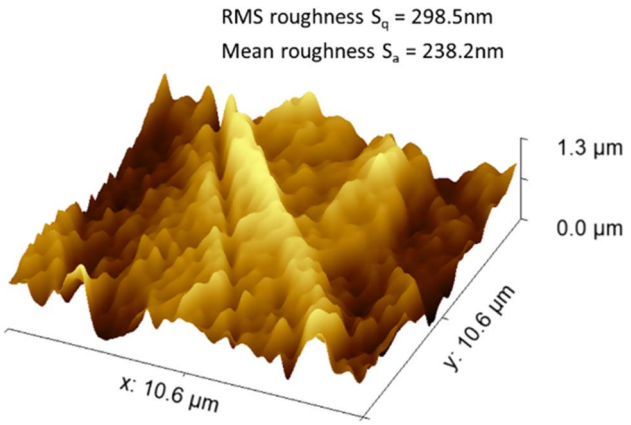

Fig. 6 AFM image and surface roughness of MGO@CA.

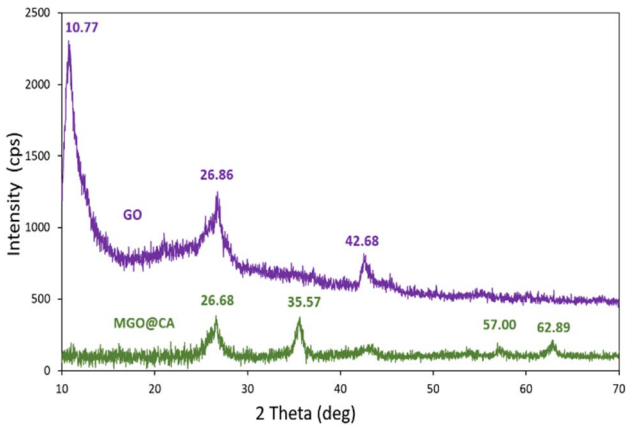

Fig. 7 XRD spectrum of GO and MGO@CA.

contribute to its high surface area, and therefore higher adsorption of molecules on it.[36]

Fig. 7 shows the XRD patterns of both GO and MGO@CA, which indicate a broad spectrum and broad peaks rather than sharp ones, revealing the more amorphous structure of the composite.[37] The 2θ peaks for GO appeared at 10.77°, 26.86°, and 42.68°, in its XRD spectrum, which indicate interlayer spacings of 0.82 nm, 0.33 nm and 0.21 nm, respectively. Alternatively, MGO@CA showed peaks at 26.68°, 35.57°, 57.00°, and 62.89°, revealing interlayer distances of 0.33 nm, 0.25 nm, 0.16 nm, 0.15 nm, respectively. The last 3 peaks at 35.57°, 57.00° and 62.89° confirm the presence of Fe_3O_4 in the composite, providing its magnetic behaviour.[38]

The surface area and pore size of the prepared mixture were determined using the Brunauer–Emmett–Teller (BET) method. The BET isotherm is represented in Fig. 8. The specific surface area and average pore diameters were determined to be 178.47 $m^2\ g^{-1}$ and 4.59 nm, respectively.

The zeta potential analysis of the magnetic composite was carried out to understand the change in surface charge with a change in solution pH. The result (Fig. 9) showed negative zeta potential values, which decreased with pH. This indicated that the surface became more negatively charged with an increase in pH.

Finally, VSM was carried out to study the magnetic properties of the prepared MGO@CA composite. Fig. 10 shows the hysteresis and remanence curve of MGO@CA having the

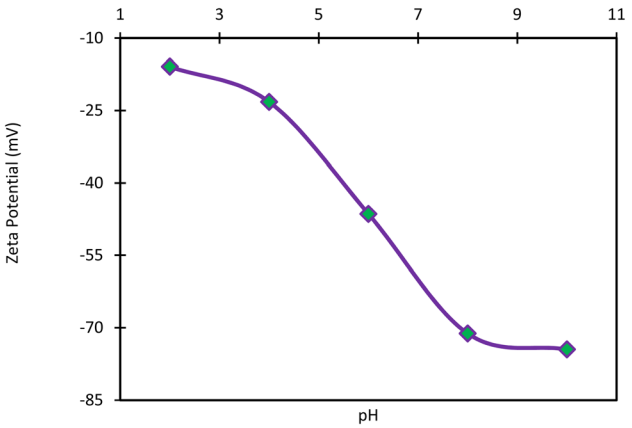

Fig. 9 Change in zeta potential with pH.

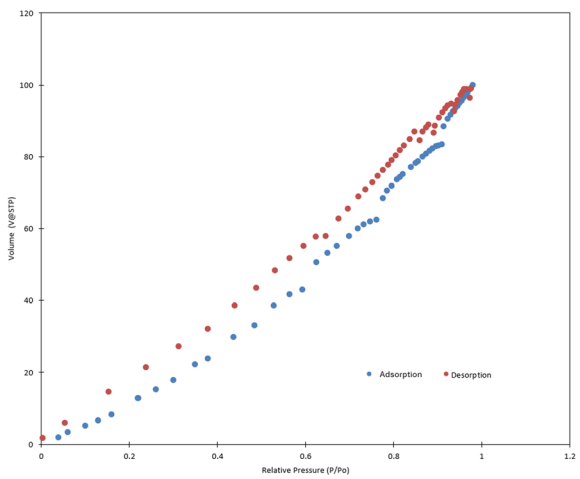

Fig. 8 BET adsorption–desorption isotherm for MGO@CA.

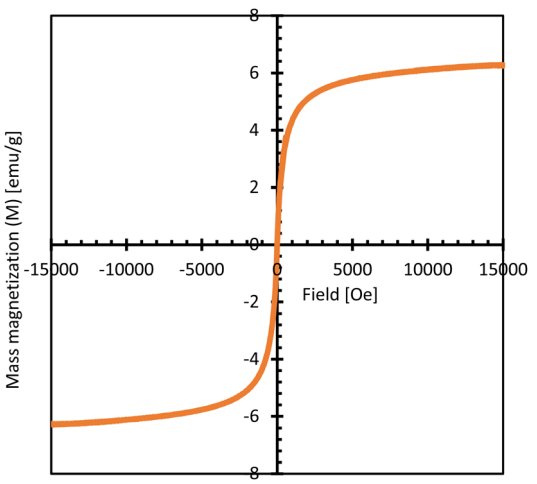

Fig. 10 Hysteresis and remanence curve of MGO@CA.

saturation magnetisation values of −6.27 emu g^{-1} and 6.26 emu g^{-1} under −15 001.13 Oe and 15 001.11 Oe external magnetic fields, respectively. These saturation values are well above 0.1 emu g^{-1}, which indicate strong ferromagnetic behaviour, and as a result the MGO@CA composite can be easily separated from aqueous mixtures using an external magnet.[39,40]

Effect of pH on adsorption of Pb on MGO@CA

The adsorption of metal ions onto different adsorbents is significantly influenced by the pH of a solution, which also affects the ionic species of metals and the surface charge of the adsorbent. The impact of altering the solution pH from 2 to 7 was investigated to understand how it affects the adsorption of lead(II) on MGO@CA, and the resultant graph is shown in Fig. 11.

The adsorption of Pb(II) was comparatively low at lower pH values, likely because of the comparative affinity between hydronium ions and heavy metal ions to the surface sites. On the surface of the adsorbent, hydronium ions were predominant in low-pH solutions. Conversely, the hydronium ion concentration decreased with an increase in the pH of the solution, creating more negatively charged sites on the composite surface. This change made it easier for cationic Pb(II) ions to bind to the surface. This was also confirmed by the zeta potential analysis, where the surface of the composite became progressively negatively charged with an increase in pH.

The graph in Fig. 11 indicates that the highest adsorption of Pb(II) occurred at pH values in the range of 5 to 7. In this range, free Pb(II) ions were more favourable for adsorption on the negative surface of the adsorbent. Conversely, when the solution pH exceeded 8, Pb(II) underwent precipitation as $Pb(OH)_2$. Thus, to ensure the optimal adsorption effectiveness and prevent Pb(II) precipitation, all investigations in this study were done at pH 6.

Effect of adsorbent dosage on adsorption of Pb by MGO@CA

By gradually increasing the adsorbent concentration from 2.5 mg/20 mL to 10 mg/20 mL, while keeping the same values for the other parameters (pH = 6, contact period = 2 h, solution concentration = 40 ppm), an investigation was conducted to assess the influence of adsorbent dosage on the adsorption of lead(II). The relationship between the amount of MGO@CA used and the proportion of lead(II) removed, as well as its adsorption capacity, was observed to be inversely correlated, as depicted in Fig. 12. The percentage of lead(II) removal from the solution varied from 96.71% to 98.53% as the adsorbent dosage increased from 2.5 mg to 10 mg. However, throughout this time, the adsorption capacity of the composite decreased from 310.11 mg g^{-1} to 78.74 mg g^{-1}. This situation is due to the increase in the adsorbent dosage, which resulted in a larger surface area and more available adsorption sites. However, the amount of metal ions adsorbed per unit of adsorbent decreased when larger quantities of adsorbent were added.

Fig. 12 clearly indicates that the concentration of 4.5 mg/20 mL serves as the intersection point of the two curves, where both adsorption capacity and percentage removal show significant values. Thus, for simplicity in further investigations, a concentration of 5 mg/20 mL was chosen as the optimum dose.

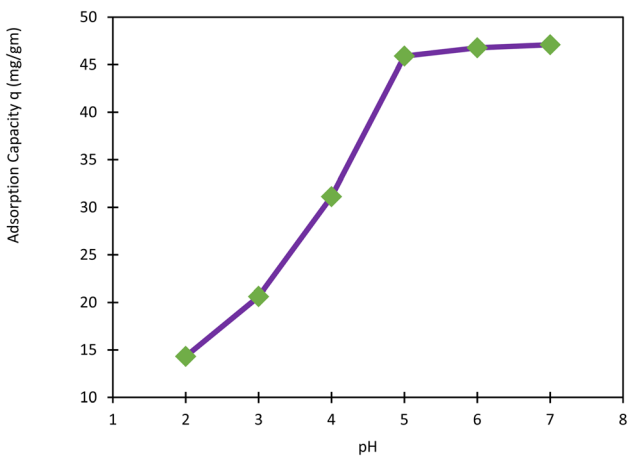

Fig. 11 Effect of pH on lead(II) adsorption on MGO@CA (5 mg/10 mL dosage, 10 ppm solution, and 301 K).

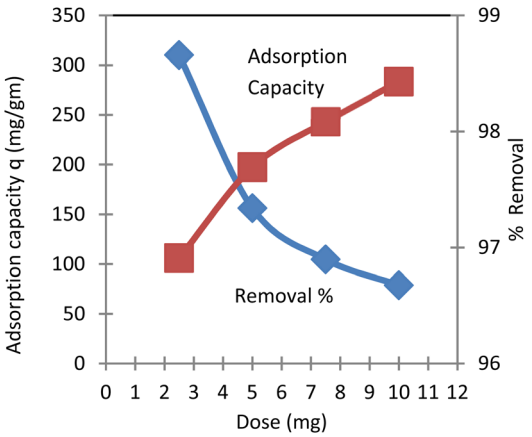

Fig. 12 Effect of adsorbent dose on lead adsorption on MGO@CA at pH 6 and 301 K.

Effect of adsorption time and initial solution concentration on adsorption of Pb on MGO@CA

This experiment examined the decrease of Pb(II) concentration over time for three initial concentrations, *i.e.*, 20, 30, and 40 ppm. The results are depicted in Fig. 13. The experiment was conducted at 301 K, with a constant pH of 6 and a fixed dosage of adsorbent of 5 mg/20 mL.

The adsorption capacity increased rapidly in the first 30 min. The initial rapid adsorption rate can be due to the many binding sites on the exterior surface of the adsorbent. Initially, heavy metal ions readily bind to these external sites. However, it may take some time for the ions to penetrate the interior regions of the adsorbent.[41]

As depicted in this figure, with an increase of the Pb concentration from 20 to 50 mg L^{-1}, the quantity of metal ions removed at equilibrium increased from 79.15 mg g^{-1} to 195.65 mg g^{-1}. This increase in adsorption capacity can be attributed to the overcoming of the mass transfer resistance between the solid phase and the aqueous solution due to the increasing concentration gradient.[42] As the concentration of the

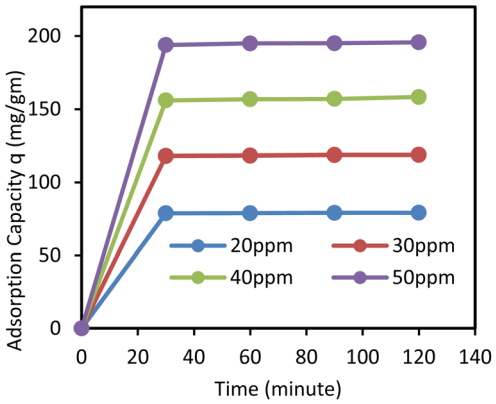

Fig. 13 Effect of adsorption time and initial solution concentration on adsorption of Pb on MGO@CA (301 K, 5 mg/20 mL dosage).

Pb^{2+} ions increases in the solution, more active sites of the composite take part in the adsorption process, and thus the adsorption capacity increases.[43]

Langmuir adsorption isotherm

The Langmuir model assumes monolayer adsorption, which was assessed using eqn (4).[44,45]

$$\frac{C_e}{q_e} = \frac{1}{q_m b} + \frac{1}{q_m} C_e \quad (4)$$

This is the linear form of Langmuir isotherm, where C_e and q_e are the concentration and adsorption capacity at equilibrium, respectively. q_m refers to the highest theoretical adsorption capacity, while b is the Langmuir constant.[46] The adsorption data resulted in a straight line, supporting monolayer adsorption.

According to the graph in Fig. 14, the highest theoretical adsorption capacity was found to be 270.27 mg g^{-1}.

Freundlich adsorption isotherm

The Freundlich adsorption model supports multilayer adsorption, where different active sites have varying adsorption energies. The adsorption data was assessed using the following equation, and the graph is shown in Fig. 15.

$$\ln q_e = \ln k_F + \frac{1}{n} \ln C_e \quad (5)$$

where k_F and n are constants. k_F indicates the theoretical capacity of the adsorbent, and n indicates the favorability of the adsorption process.[47]

The values of n and k_F were calculated to be 1.79 and 188.18, respectively. The linear form of the isotherm, as well as the values of n and k_F support multilayer adsorption.[48] The adsorption data fits both models, which indicates that the adsorbent has regions with different adsorption energies, leading to a combination of monolayer and multilayer adsorption.[49]

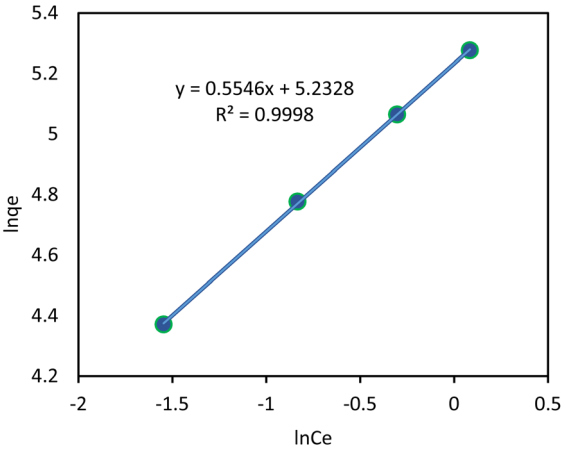

Fig. 15 Freundlich adsorption isotherm for the adsorption of Pb on MGO@CA (301 K and 5 mg/20 mL dosage).

Adsorption kinetics

The adsorption data was analysed using the pseudo-first-order and pseudo-second-order models to assess the kinetics of the adsorption process using the following equations:[44,45]

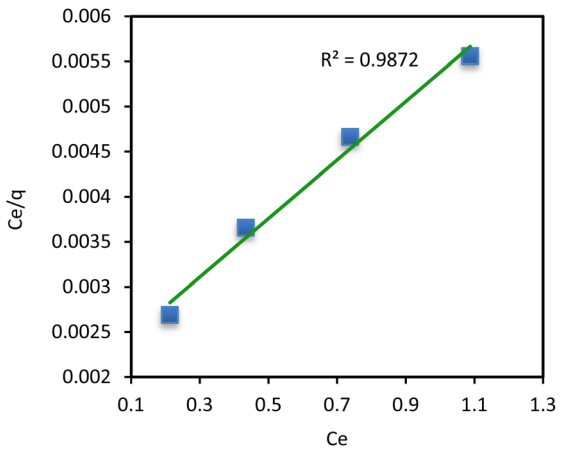

Fig. 14 Langmuir adsorption isotherm for the adsorption of Pb on MGO@CA (301 K and 5 mg/20 mL dosage).

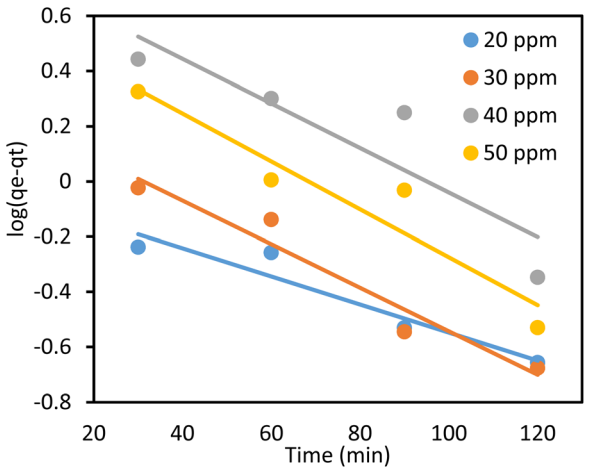

Fig. 16 Pseudo-first-order adsorption kinetics for the adsorption of Pb on MGO@CA at 301 K.

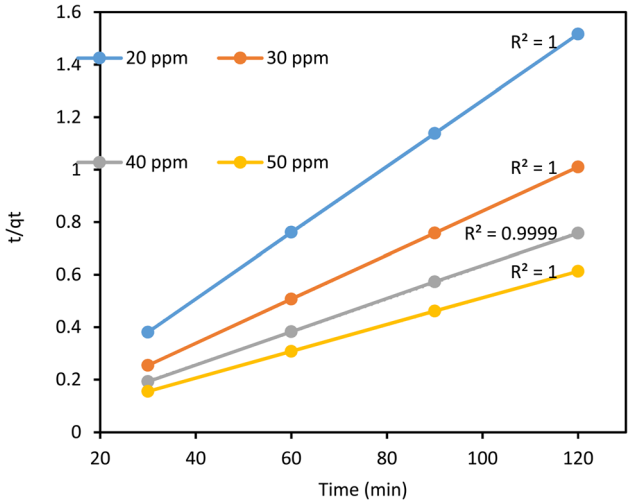

Fig. 17 Pseudo-second-order adsorption kinetics for the adsorption of Pb on MGO@CA at 301 K.

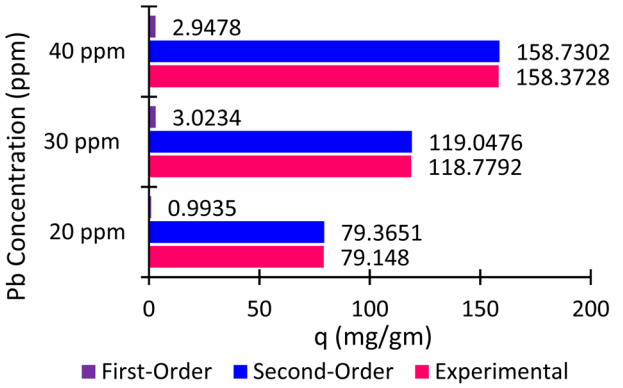

Fig. 18 Comparison of adsorption capacities of pseudo-first-order, pseudo-second-order and experimental for Pb on MGO@CA.

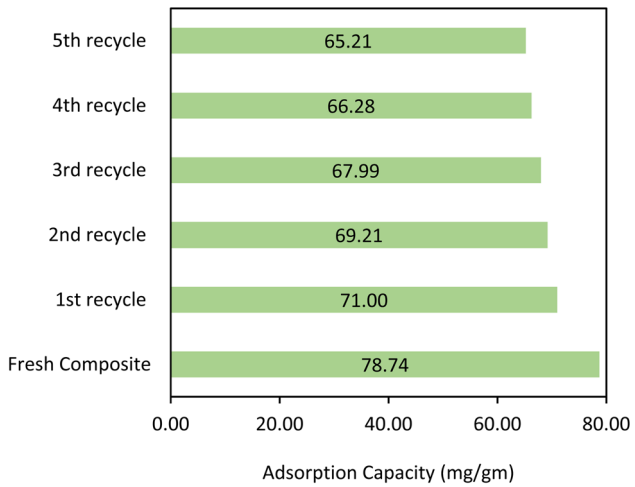

Fig. 19 Regeneration study of MGO@CA up to the 5th recycle (pH = 6, 10 mg/20 mL dosage, and 2 h).

$$\text{Pseudo-first-order}: \log(q_e - q_t) = \log q_e - \frac{k_1}{2.303} t \quad (6)$$

$$\text{Pseudo-second-order}: \frac{t}{q_t} = \frac{1}{k_2 q_e^2} + \frac{1}{q_e} t \quad (7)$$

where q_e = equilibrium adsorption capacity, q_t = adsorption capacity at time t, k_1 = rate constant of pseudo-first-order adsorption (L min^{-1}), and k_2 = the rate constant of pseudo-second order adsorption (g mg^{-1} min^{-1}).

Fig. 16 and 17 represent the graph of the reaction kinetics.

The adsorption data exhibited a stronger fit with the pseudo-second-order kinetics (Fig. 17). Thus, the adsorption process

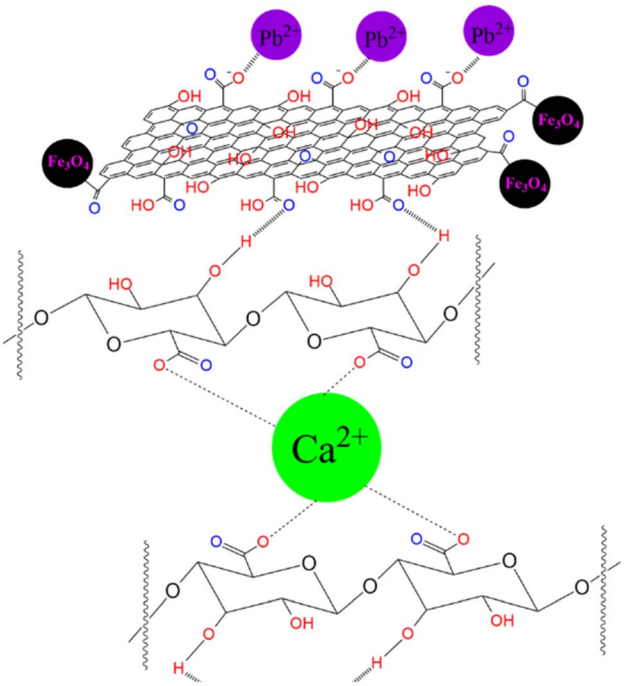

Fig. 20 Schematic representation of the proposed mechanism for the adsorption of Pb on MGO@CA.

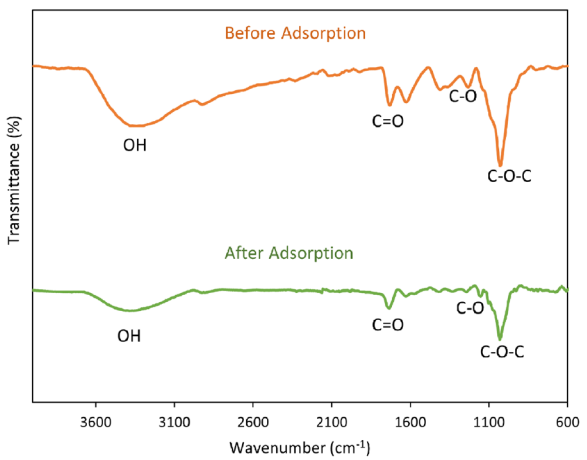

Fig. 21 FTIR spectrum of MGO@CA before and after adsorption.

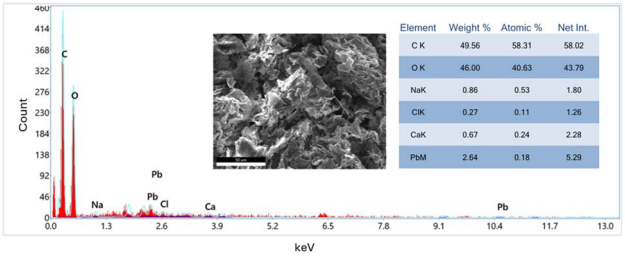

Fig. 22 EDX graph of MGO@CA after adsorption.

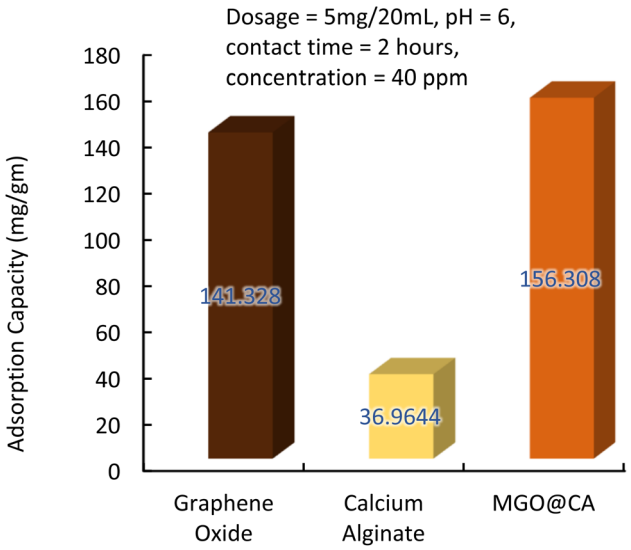

Fig. 23 Adsorption capacities of graphene oxide, calcium alginate and the MGO@CA composite.

depends not only on the concentration of the adsorbent but also on the initial concentration of the metal ions.[50] This result is also supported by the adsorption time and initial concentration data, which showed that a higher initial concentration resulted in higher adsorption capacity. A comparison between the experimental adsorption capacities with the adsorption capacities obtained from pseudo-first-order and pseudo-second-order kinetic models is shown in Fig. 18. It can be clearly seen that the experimental data is closer to the theoretical values calculated from the pseudo-second-order reaction kinetics.

Regeneration study

The MGO@CA composite was regenerated by washing the used adsorbent with 4% HCl solution several times. Then, the composite was washed with distilled water several times to neutralize the pH. The results from the regeneration study (Fig. 19) confirmed the reusability and stability of the composite as an adsorbent. The composite retained 82.28% of its initial adsorption capacity after the 5th recycle.

Plausible mechanism

According to the FTIR spectrum (Fig. 2), it is evident that carboxyl and hydroxyl groups were present on the surface of the MGO@CA composite, and these groups became dissociated when exposed to an aqueous solution, resulting in the formation of a negatively charged surface. The presence of negative charge on the surface was confirmed by the zeta potential analysis (Fig. 9). Because of electrostatic attraction, the Pb^{2+} cations will be drawn to the negatively charged surface of the MGO@CA beads. These ions will either stick to the surface or transport into the interior of the composite. Consequently, the composite demonstrated very high adsorption capabilities in the presence of positively charged Pb^{2+} ions. The mechanism is schematically shown in Fig. 20.

Fig. 21 shows the FTIR spectrum of the MGO@CA adsorbent before and after the adsorption experiment. The reduction in the FTIR peak intensity after adsorption suggests that the functional groups were involved in the adsorption process, which means they successfully latched onto the positively charged ions. Given that the active sites were blocked by the adsorbed dye molecules, they were less free to interact with IR radiation, and as a result their intensity was reduced.

The adsorption of Pb^{2+} was also confirmed by the EDX analysis carried onto the adsorbent after the adsorption process. The spectrum and data shown in Fig. 22 indicate the presence of a significant amount (2.64 weight%) of Pb^{2+} on the composite after adsorption, which was not recorded in the EDX spectrum before adsorption (Fig. 4).

Fig. 23 depicts the adsorption capacities of graphene oxide, calcium alginate and MGO@CA composite. MGO@CA showed a higher adsorption capacity than other two materials, which were used for synthesising the composite.

The maximum adsorption capacity for Pb of some other materials is given in Table 1. It is evident from the table that MGO@CA performed really well in removing Pb^{2+} from an aqueous system.

Table 1 Comparison of lead adsorption by different composites

Name of the composite	Maximum adsorption capacity	Reference
Organic ligand-embedded large-pore facial composite materials	176.66 mg g^{-1}	51
Sustainable biochar derived from poplar saw dust	62.68 mg g^{-1}	52
Magnetic oak wood ash/graphene oxide (ash/GO/Fe_3O_4) nanocomposites	47.16 mg g^{-1}	53
Magnetic chitosan/graphene oxide composites	76.94 mg g^{-1}	54
Hydrophilic biochar obtained by an acid ammonium persulfate oxidation (nZVI-HPB)	135.4 mg g^{-1}	55
Magnetic graphene oxide calcium alginate composite	270.27 mg g^{-1}	This study

Conclusions

A composite (MGO@CA) was synthesised successfully and characterised using multiple techniques, including FTIR, FESEM, XRD, EDX, TEM, AFM, BET, and VSM, which confirmed the presence of graphene oxide, magnetic iron oxide nanoparticles, and sodium alginate with calcium carbonate cross-linking. This study investigated several doses of MGO@CA, ranging from 2.5 mg to 10 mg. The adsorption of Pb^{2+} ions was greatly affected by the solution pH, with the most favourable adsorption taking place at pH 6. The maximum theoretical adsorption capacity, as determined by the Langmuir isotherm model, was 270.27 mg g^{-1}. This value represents the upper limit of the lead ion adsorption per gram of the composite material when the conditions were optimised. The adsorption data fit both the Langmuir and Freundlich adsorption isotherms, indicating homogeneous and heterogeneous surface characteristics. The adsorption process followed the pseudo-second-order reaction kinetics. The high surface area and negative surface charge of the prepared composite are the plausible reasons for its high adsorption capacity. This discovery yields a stable and highly effective adsorbent material for efficiently eliminating Pb^{2+} ions from wastewater.

Data availability

The data supporting this article have been included as part of the ESI.†

Author contributions

Sadit Bihongo Malitha: writing-original draft, investigation, methodology, formal analysis, data curation, validation, software, funding acquisition; Dewan Md. Mahmudunnabi: writing-review & editing, methodology, validation, supervision; Shreyoshi Mazumder: writing-review & editing, investigation, software; Khandker Saadat Hossain: investigation, software, validation; Mohammad Nurnabi: project administration, supervision, visualization; Md. Zahangir Alam: supervision, resources, funding acquisition, project administration, visualization.

Conflicts of interest

The authors declare that they do not have any conflict of interest or any kind of competing interest.

Acknowledgements

The research was supported by the Semiconductor Technology Research Centre (STRC), the University of Dhaka (DU), and the Bangladesh Council of Scientific and Industrial Research (BCSIR). The authors would like to thank Md. Saiful Quddus (Senior Scientific Officer, IGCRT, BCSIR), Hridoy Roy (Lecturer, Department of Chemical Engineering, Bangladesh University of Engineering & Technology), Aqib Ash Shaheed Siddique Tarif and Mr Md. Mazharul Hoque (Executive Engineer, ACCE, DU), for their warm assistance in BET, AAS, SEM-EDX, and UV analysis.

References

1 C. Zamora-Ledezma, D. Negrete-Bolagay, F. Figueroa, E. Zamora-Ledezma, M. Ni, F. Alexis and V. H. Guerrero, *Environ. Technol. Innovation*, 2021, **22**, 101504.
2 S. S. Sonone, S. Jadhav, M. Singh Sankhla and R. Kumar, *Review*, 2021, **10**, 2148–2166.
3 K. Ahmad, H. U. R. Shah, H. A. Nasim, A. Ayub, M. Ashfaq, A. Rauf, S. S. A. Shah, M. M. Ahmad, H. Nawaz and E. Hussain, *Toxin Rev.*, 2022, **41**, 577–587.
4 A. Carocci, A. Catalano, G. Lauria, M. S. Sinicropi and G. Genchi, *Rev. Environ. Contam. Toxicol.*, 2016, **238**, 45–67.
5 U. Zulfiqar, M. Farooq, S. Hussain, M. Maqsood, M. Hussain, M. Ishfaq, M. Ahmad and M. Z. Anjum, *J. Environ. Manage.*, 2019, **250**, 109557.
6 F. Hadi and T. Aziz, *Journal of Biology and Life Science*, 2015, **6**, 91.
7 J. Pandiyan, S. Mahboob, M. Govindarajan, K. A. Al-Ghanim, Z. Ahmed, N. Al-Mulhm, R. Jagadheesan and K. Krishnappa, *Saudi J. Biol. Sci.*, 2021, **28**, 1218–1225.
8 M. A. T. M. T. Rahman, M. Paul, N. Bhoumik, M. Hassan, M. K. Alam and Z. Aktar, *Appl. Water Sci.*, 2020, **10**, 1–15.
9 M. Kader, D. T. Lamb, K. R. Mahbub, M. Megharaj and R. Naidu, *Environ. Sci. Pollut. Res.*, 2016, **23**, 15460–15470.
10 M. Bongers, B. Rusch and C. A. M. Van Gestel, *Environ. Toxicol. Chem.*, 2004, **23**, 195–199.
11 L. Zhang and C. A. M. Van Gestel, *Environ. Pollut.*, 2019, **247**, 866–873.
12 A. K. Majumder, A. Al Nayeem, M. Islam, M. M. Akter and W. S. Carter, *J. Health Pollut.*, 2021, **11**, 1–21.
13 M. Z. Islam and M. G. Mostafa, *Water Pract. Technol.*, 2024, **19**(3), 745–760.
14 A. Saravanan, P. Senthil Kumar, S. Jeevanantham, S. Karishma, B. Tajsabreen, P. R. Yaashikaa and B. Reshma, *Chemosphere*, 2021, **280**, 130595.
15 D. Dutta, S. Arya and S. Kumar, *Chemosphere*, 2021, **285**, 131245.
16 A. Saravanan, P. S. Kumar, R. V. Hemavathy, S. Jeevanantham, M. J. Jawahar, J. P. Neshaanthini and R. Saravanan, *Chemosphere*, 2022, **307**, 135713.
17 K. Ul Khair, K. Ahmad, M. Kashif, K. Naseem, K. Qureshi and H. Majeed, *Rev. Inorg. Chem.*, 2024, **44**, 671–684.
18 K. Ahmad, M. A. Nazir, A. K. Qureshi, E. Hussain, T. Najam, M. S. Javed, S. S. A. Shah, M. K. Tufail, S. Hussain, N. A. Khan, H. ur R. Shah and M. Ashfaq, *Mater. Sci. Eng., B*, 2020, **262**, 114766.
19 K. Ahmad, H. ur R. Shah, M. Ashfaq, S. S. A. Shah, E. Hussain, H. A. Naseem, S. Parveen and A. Ayub, *Food Chem. Toxicol.*, 2021, **149**, 112008.
20 F. Farjadian, S. Abbaspour, M. A. A. Sadatlu, S. Mirkiani, A. Ghasemi, M. Hoseini-Ghahfarokhi, N. Mozaffari, M. Karimi and M. R. Hamblin, *ChemistrySelect*, 2020, **5**, 10200–10219.

21 D. Y. Kornilov and S. P. Gubin, *Russ. J. Inorg. Chem.*, 2020, **65**(13), 1965–1976.
22 W. Wu, Y. Shi, G. Liu, X. Fan and Y. Yu, *Desalination*, 2020, **491**, 114452.
23 P. Kumari, K. M. Tripathi, L. K. Jangir, R. Gupta and K. Awasthi, *Mater. Today Chem.*, 2021, **22**, 100597.
24 H. Yu, Y. He, G. Xiao, Y. Fan, J. Ma, Y. Gao, R. Hou, X. Yin, Y. Wang and X. Mei, *Chem. Eng. J.*, 2020, **389**, 124375.
25 K. Y. Lee and D. J. Mooney, *Prog. Polym. Sci.*, 2012, **37**, 106–126.
26 W. B. Zhao, M. R. Du, K. K. Liu, R. Zhou, R. N. Ma, Z. Jiao, Q. Zhao and C. X. Shan, *ACS Appl. Mater. Interfaces*, 2020, **12**, 13305–13315.
27 X. Gao, C. Guo, J. Hao, Z. Zhao, H. Long and M. Li, *Int. J. Biol. Macromol.*, 2020, **164**, 4423–4434.
28 Y. Zhu, S. Murali, W. Cai, X. Li, J. W. Suk, J. R. Potts and R. S. Ruoff, *Adv. Mater.*, 2010, **22**, 3906–3924.
29 S. B. Malitha, D. M. Mahmudunnabi, M. Nurnabi and M. Z. Alam, *Water, Air, Soil Pollut.*, 2023, **234**, 1–17.
30 A. Sharif, M. Khorasani and F. Shemirani, *J. Inorg. Organomet. Polym. Mater.*, 2018, **28**, 2375–2387.
31 D. M. Mahmudunnabi, M. Z. Alam and M. Nurnabi, *Desalin. Water Treat.*, 2020, **174**, 389–399.
32 Y. G. Luan, X. A. Zhang, S. L. Jiang, J. H. Chen and Y. F. Lyu, *Chin. J. Polym. Sci.*, 2018, **36**, 584–591.
33 J. Yan, K. Li, J. Yan, Y. Fang and B. Liu, *Appl. Surf. Sci.*, 2022, **602**, 154338.
34 R. Rashidi, S. Khakpour, S. Masoumi and Y. Jafarzadeh, *Chem. Eng. Res. Des.*, 2022, **177**, 815–825.
35 G. A. Kloster, D. Muraca, O. Moscoso Londoño, K. R. Pirota, M. A. Mosiewicki and N. E. Marcovich, *Composites, Part A*, 2020, **135**, 105936.
36 P. S. Gauna, A. A. G. Blanco, D. Barrera, J. Villarroel-Rocha, J. P. Hinestroza, M. Kimura, M. L. Kim, E. H. Otal and K. Sapag, *Adsorption*, 2023, **29**, 351–361.
37 H. Sanaeepur, R. Ahmadi, M. Sinaei and A. Kargari, *J. Membr. Sci. Res.*, 2019, **5**, 25–32.
38 E. A. Namikuchi, R. D. L. Gaspar, D. S. Da Silva, I. M. Raimundo and I. O. Mazali, *Nano Express*, 2021, **2**, 020022.
39 B. Sun, Z. Yan, Y. Cao, S. Ding, R. Li, B. Ma, X. Y. Li, H. Yang, W. Yin, Y. Zhang, Q. Wang, X. Shao, D. Yang, D. Xue and H. L. Zhang, *Adv. Mater.*, 2023, **35**, 2303945.
40 Y. Liu, H. Zhang, Q. Zhao, Q. Lu, M. Zhu and M. Zhang, *Phys. Chem. Chem. Phys.*, 2019, **21**, 15089–15096.
41 M. K. Ubhi, M. Kaur, D. Singh and V. K. Sharma, *J. Water Process Eng.*, 2023, **52**, 103539.
42 S. Singh, B. U, T. S. S. Kumar Naik, S. K. Behera, N. A. Khan, J. Singh, L. Singh and P. C. Ramamurthy, *Environ. Res.*, 2023, **216**, 114750.
43 A. M. Omer, M. El-Sayed, E. M. Abd El-Monaem, G. M. El-Subruiti and A. S. Eltaweil, *Int. J. Biol. Macromol.*, 2023, **253**, 127437.
44 J. Palit, S. B. Malitha, M. A. S. Mia and M. Z. Alam, *Adsorption*, 2024, **30**, 1971–1984.
45 D. M. Mahmudunnabi, M. Z. Alam and M. Nurnabi, *Desalin. Water Treat.*, 2024, **319**, 100459.
46 Q. Wang, D. Liang, Y. Yang, Y. Zhang, Y. Wang, L. Zhang, R. Ma and Z. Niu, *RSC Adv.*, 2024, **14**, 23483–23494.
47 M. Ebato, K. Yonebayashi and T. Kosaki, *Soil Sci. Plant Nutr.*, 2001, **47**, 221–231.
48 S. Panahi, A. Reza Sardarian, F. Esmaeilzadeh, K. Kim, K. Lee, S. So, M. Firdaus, S. Wahyuningsih, F. Rahmawati and T. Kusumaningsih, *IOP Conf. Ser.: Mater. Sci. Eng.*, 2020, **858**, 012010.
49 T. S. Khayyun and A. H. Mseer, *Appl. Water Sci.*, 2019, **9**, 1–8.
50 A. Turner and L. A. Holmes, *Environ. Chem.*, 2015, **12**, 600–610.
51 M. R. Awual, M. M. Hasan, J. Iqbal, A. Islam, M. A. Islam, A. M. Asiri and M. M. Rahman, *Microchem. J.*, 2020, **154**, 104585.
52 S. Cheng, Y. Liu, B. Xing, X. Qin, C. Zhang and H. Xia, *J. Cleaner Prod.*, 2021, **314**, 128074.
53 R. Pelalak, Z. Heidari, S. M. Khatami, T. A. Kurniawan, A. Marjani and S. Shirazian, *Arabian J. Chem.*, 2021, **14**, 102991.
54 L. Fan, C. Luo, M. Sun, X. Li and H. Qiu, *Colloids Surf., B*, 2013, **103**, 523–529.
55 S. Li, F. Yang, J. Li and K. Cheng, *Sci. Total Environ.*, 2020, **746**, 141037.